Diffuse-interface modeling of liquid-vapor coexistence in equilibrium drops using smoothed particle hydrodynamics

Leonardo Di G. Sigalotti,[*] Jorge Troconis,[†] Eloy Sira,[‡] and Franklin Peña-Polo[§]
Centro de Física, Instituto Venezolano de Investigaciones Científicas, IVIC, Apartado Postal 20632, Caracas 1020-A, Venezuela

Jaime Klapp[‖]
Departamento de Física, Instituto Nacional de Investigaciones Nucleares, ININ, Km. 36.5, Carretera México-Toluca, 52750, La Marquesa, Estado de México, Mexico and Departamento de Matemáticas, Cinvestav del Instituto Politécnico Nacional (I.P.N.), 07360, México City, Mexico

(Received 17 February 2014; published 28 July 2014)

We study numerically liquid-vapor phase separation in two-dimensional, nonisothermal, van der Waals (vdW) liquid drops using the method of smoothed particle hydrodynamics (SPH). In contrast to previous SPH simulations of drop formation, our approach is fully adaptive and follows the diffuse-interface model for a single-component fluid, where a reversible, capillary (Korteweg) force is added to the equations of motion to model the rapid but smooth transition of physical quantities through the interface separating the bulk phases. Surface tension arises naturally from the cohesive part of the vdW equation of state and the capillary forces. The drop models all start from a square-shaped liquid and spinodal decomposition is investigated for a range of initial densities and temperatures. The simulations predict the formation of stable, subcritical liquid drops with a vapor atmosphere, with the densities and temperatures of coexisting liquid and vapor in the vdW phase diagram closely matching the binodal curve. We find that the values of surface tension, as determined from the Young-Laplace equation, are in good agreement with the results of independent numerical simulations and experimental data. The models also predict the increase of the vapor pressure with temperature and the fitting to the numerical data reproduces very well the Clausius-Clapeyron relation, thus allowing for the calculation of the vaporization pressure for this vdW fluid.

DOI: 10.1103/PhysRevE.90.013021 PACS number(s): 47.55.−t, 47.11.−j, 64.75.−g, 05.70.−a

I. INTRODUCTION

When a homogeneous solution of a given composition is quenched to below the critical temperature into the unstable region of the phase diagram, bounded by the *coexistence* (or *binodal*) curve, the separation of the solution into two different phases may occur either by nucleation or by spinodal decomposition. In general, many of the basic features of phase transitions can be understood in the framework of the van der Waals (vdW) mean-field theory of capillarity [1]. For instance, nucleation occurs when quenching takes the solution into the metastable region enclosed by the binodal and *spinodal* curves, where the system is thermodynamically unstable to the growth of large fluctuations only. In contrast, when the system crosses the locus defined by the spinodal curve into the unstable region, phase separation occurs spontaneously without the presence of a nucleation step. This process, known as *spinodal decomposition*, results in phase separation even for infinitesimally small fluctuations with a high interconnectivity of the two phases [2].

The subject of spinodal decomposition has been reviewed in depth by many authors [3–6] and much of the current interest in this field is generated by the utility of several alloy systems whose properties are a consequence of this mode of decomposition [7,8]. Spinodal decomposition has also been observed in a variety of other materials such as mineral glasses, mineral solid solutions in geology, steels, gels, ceramics, and mixtures of polymers and liquids [9–11]. When these systems are quenched from an initial stable state into one inside the miscibility gap of the phase diagram, they become unstable against statistical fluctuations that restore equilibrium, forming during the process a transient pattern of concentration inhomogeneities. Since the introduction of the concept of the growth of fluctuations by Cahn and Hilliard [12,13], there has been an increasing interest in understanding the dynamics of pattern formation by means of computer simulation models [14–21].

In this paper, we are primarily concerned with numerical simulations of liquid-vapor spinodal decomposition in two-dimensional (2D), nonisothermal, van der Waals drops formed from an initial square-shaped liquid, using the method of smoothed particle hydrodynamics (SPH). While most previous simulations of liquid-vapor phase separation systems has focused on studying spinodal decomposition in an infinite expanse of fluid with periodic boundary conditions, only very few computer models have been reported in the literature dealing with spinodal decomposition in liquid drops [22–24]. In particular, Nugent and Posch [22] performed SPH simulations of a gas-liquid phase transition in subcritical drops using a vdW equation of state. In their models, surface tension is not an input parameter because it arises naturally from the attractive (cohesive) part of the vdW equation of state. In fact, near the gas-liquid interface, the attractive, long-range,

[*]leonardo.sigalotti@gmail.com
[†]jorge.troconis@gmail.com
[‡]Corresponding author: esira.ivic@gmail.com
[§]franklin.pena@gmail.com
[‖]jaime.klapp@inin.gob.mx

interparticle interaction is different between the two phases, producing a surface force perpendicular to the surface itself and pointing toward the denser phase. Therefore, in this approach there is no need to explicitly locate the surface, and then to calculate the local surface curvature. In contrast, our approach uses a vdW equation of state combined with the diffuse-interface model for a single-component fluid [25], where a stress (Korteweg) tensor, as derived from the Helmholtz free energy functional, is added to the viscous stress in the momentum equation to model the rapid but smooth transition of physical quantities through the interface separating the bulk phases [25]. This body force is a reversible one and is driven by the density gradients in the fluid, resulting in spontaneous phase separation and surface tension. Therefore, inherent in this formulation is an interfacial width that is determined by the length scale over which the density changes. Moreover, at the late stages of phase separation away from the critical point, when the liquid is separated from the vapor by a sharp interface, the Korteweg force reduces essentially to the Marangoni force [26,27]. In this sharp-interface limit, it can be shown that the interfacial thickness approaches asymptotically the free-boundary formulation, where the intervening interface between the bulk fluids is represented by a surface of zero thickness endowed with physical properties such as surface tension [25].

The plan of the paper is as follows. The governing equations are described in Sec. II. In Sec. III we outline the numerical method and derive stable SPH representations for the components of the nonequilibrium Korteweg force. In Sec. IV we present the results of the numerical simulations for a sequence of forming drops undergoing spinodal decomposition for a range of densities and temperatures. We first show that the equilibrium densities and temperatures on the vapor-liquid interface are predicted by the model in accordance with the Maxwell construction tie-line. Second, we calculate the surface properties of the vdW drops and compare the dependence of the surface tension on temperature to previous simulations and experimental measurements. Finally, Sec. V summarizes the conclusions.

II. BASIC EQUATIONS AND FORMULATION

The diffuse-interface theory has been developed mainly to describe the motion of a fluid near its critical point [25]. However, it has also been applied to situations away from the critical point, where the interfacial thickness approaches asymptotically that of a free boundary. For general, nonequilibrium conditions, the motion of a compressible, viscous, heat-conducting, single-component fluid near its critical point and in the absence of external forces is described by the solution of the local conservation laws:

$$\frac{d\rho}{dt} = -\rho\nabla\cdot\mathbf{v}, \tag{1}$$

$$\frac{d\mathbf{v}}{dt} = \frac{1}{\rho}\nabla\cdot(\mathbb{T}+\mathbb{K}), \tag{2}$$

$$\frac{dU}{dt} = \frac{1}{\rho}\mathbb{T}:\nabla\mathbf{v} - \frac{1}{\rho}\nabla\cdot\mathbf{q}, \tag{3}$$

where ρ is the mass density, $\mathbf{v}$ is the velocity vector, U is the specific internal energy, and d/dt denotes the total derivative with respect to time t. In the above equations $\mathbb{T}$ and $\mathbf{q}$ are the viscous stress tensor and the heat-flux vector, given by

$$\mathbb{T} = -p\mathbb{I} + \eta(\nabla\mathbf{v} + \nabla\mathbf{v}^t) + \left(\zeta - \frac{2}{d}\eta\right)(\nabla\cdot\mathbf{v})\mathbb{I}, \tag{4}$$

and

$$\mathbf{q} = -\kappa\nabla T, \tag{5}$$

respectively, where the superscript t in Eq. (4) denotes transposition, p is the isotropic pressure, T is the fluid temperature, η is the shear viscosity, ζ is the bulk viscosity, κ is the coefficient of heat conduction, d is the spatial dimension ($d = 2$ for 2D flows), and $\mathbb{I}$ is the identity tensor. In Eq. (2), $\mathbb{K}$ represents the reversible part of the stress tensor expressed in terms of the nonequilibrium Korteweg tensor [25,28]

$$\mathbb{K} = K\left(\rho\nabla^2\rho + \tfrac{1}{2}|\nabla\rho|^2\right)\mathbb{I} - K\nabla\rho\nabla\rho, \tag{6}$$

where K is the gradient energy coefficient, which, for simplicity, we assume to be constant. For a nonuniform single-component fluid in equilibrium, the form of the Korteweg tensor can be derived by minimizing the Helmholtz free energy functional subject to a constraint of constant mass [25]. The presence of this nonclassical term in the momentum equation (2) for a two-fluid system allows to model the effects of capillary forces associated with a diffuse interface. It replaces the infinitely thin interface of classical models with a diffuse one which is determined by the continuous variations of an order parameter (such as the density) in a way that is consistent with microscopic theories of the interface.

Constitutive equations for the pressure and specific internal energy must be supplied to close Eqs. (1) to (3). As in Ref. [22], we adopt the vdW equations of state

$$p = \frac{\rho\bar{k}_B T}{1-\bar{\beta}\rho} - \bar{\alpha}\rho^2, \tag{7}$$

and

$$U = \frac{\xi}{2}\bar{k}_B T - \bar{\alpha}\rho, \tag{8}$$

which can be used to model the behavior of the fluid under consideration. These equations were derived from statistical mechanics as the mean-field limit for the free energy density of a system of hard particles of radius r_0 with a superimposed long-range, attractive pair potential. Here $\bar{k}_B = k_B/m$, $\bar{\alpha} = \alpha/m^2$, $\bar{\beta} = \beta/m$, and ξ is the number of degrees of freedom for the particles, where k_B is the Boltzmann's constant, α controls the strength of the attractive force, β is a constant parameter that relates to the size of the particle, and m is the particle mass. In two dimensions, $\beta = 2\pi r_0^2$ and $\xi = 2$. The vdW equations of state are realistic to display a liquid-to-gas phase transition similar to that of a real fluid, while the attractive, interparticle interaction force implicit in the cohesive term results in a surface tension. In fact, the equilibrium density profile obtained using Eqs. (6) and (7) represents a smooth transition from one bulk density to the other over a length scale associated with the gradient energy coefficient K. Identifying the surface energy of the liquid-vapor interface at local equilibrium with

the surface tension coefficient σ, we have that [20,29]

$$\sigma = K \int_0^\infty (\nabla\rho)^2 dl, \tag{9}$$

where dl is a line element. Hence, $\sigma\delta$ is an estimate of the interfacial energy, where δ is the characteristic thickness of the interface.

III. SPH EQUATIONS

We use standard SPH, modified with an adaptive density kernel estimation procedure [30], to solve Eqs. (1) to (3). Details of the method can be found in Refs. [31–33], where it has been applied to model finite-amplitude drop oscillations, drop condensation for a vdW fluid, and compressible flows with strong shocks.

SPH is a fully Lagrangian, mesh-free method in which the fluid is represented by a distribution of particles. A particle is defined to represent a finite volume in continuum scale and the field variables (and their derivatives) are evaluated at the position of particles in continuous form by means of a kernel approximation, which in SPH form is replaced by a summation over all neighboring particles [34]. With this provision, the density at particle i can be written as

$$\rho_i = \sum_{j=1}^{N} m_j W_{ij}, \tag{10}$$

where m_j is the mass of the neighbor particle j, $W_{ij} = W(|\mathbf{x}_i - \mathbf{x}_j|, h)$ is the kernel (or smoothing) function, and h is the smoothing length. The summation is taken over all N particles in the support domain of particle i, including it. Equation (10) conserves mass exactly and in most SPH applications it replaces the continuity equation (1).

To preserve variational consistency of the full SPH scheme, the use of Eq. (10) requires the use of symmetrized SPH representations for the momentum and thermal energy equations [35]

$$\frac{d\mathbf{v}_i}{dt} = \sum_{j=1}^{N} m_j \left(\frac{\mathbb{T}'_i}{\rho_i^2} + \frac{\mathbb{T}'_j}{\rho_j^2}\right) \cdot \nabla_i W_{ij} + 2\bar{\alpha} \sum_{j=1}^{N} m_j \nabla_i W_{ij}^H + \sum_{j=1}^{N} m_j \left(\frac{\mathbb{K}_i^H}{\rho_i^2} + \frac{\mathbb{K}_j^H}{\rho_j^2}\right) \cdot \nabla_i W_{ij}^H, \tag{11}$$

$$\frac{dU_i}{dt} = \frac{1}{2} \sum_{j=1}^{N} m_j \left(\frac{\mathbb{T}'_i}{\rho_i^2} + \frac{\mathbb{T}'_j}{\rho_j^2}\right) : (\mathbf{v}_j - \mathbf{v}_i) \nabla_i W_{ij} + \bar{\alpha} \sum_{j=1}^{N} m_j (\mathbf{v}_j - \mathbf{v}_i) \cdot \nabla_i W_{ij}^H - \sum_{j=1}^{N} m_j \left(\frac{\mathbf{q}_i}{\rho_i^2} + \frac{\mathbf{q}_j}{\rho_j^2}\right) \cdot \nabla_i W_{ij}, \tag{12}$$

where $\mathbb{T}' = \mathbb{T} - \bar{\alpha}\rho^2\mathbb{I}$ and $W_{ij}^H = W(|\mathbf{x}_i - \mathbf{x}_j|, H)$ with $H \geqslant 2h$. Equations (10) to (12) must be integrated simultaneously with the equation

$$\frac{d\mathbf{x}_i}{dt} = \mathbf{v}_i, \tag{13}$$

for the instantaneous positions of particles. As was first noticed by Nugent and Posch [22], we must distinguish between the short-range and the long-range components of the vdW equation of state to obtain stable circular drops and handle surface tension effects properly. Since the cohesive term $-\bar{\alpha}\rho^2$ in Eq. (7) is responsible for an attractive, long-range, central force acting between the SPH particles, and since these forces largely cancel in the bulk phases except in the neighborhood of the phase boundary, improved interfacial stability with SPH would demand increasing their interaction range to H compared to h for all other forces entering the SPH equations of motion. A similar provision is taken for the cohesive contribution to heating in the thermal energy equation. The same is also true for the Korteweg force in Eq. (11), where $\mathbb{K}^H$ means that the density and its gradients in the smoothed representation of $\mathbb{K}$ must also be calculated using a longer smoothing length to obtain well-behaved liquid-vapor coexistence with SPH and avoid the appearance of unstable attractive forces between particles for some densities and temperatures [36].

The gradient and divergence of the velocity field involved in the definition of the viscous stress tensor (4) are evaluated using the SPH summations

$$(\nabla\mathbf{v})_i = \sum_{j=1}^{N} \frac{m_j}{\rho_{ij}} (\mathbf{v}_j - \mathbf{v}_i) \nabla_i W_{ij}, \tag{14}$$

and

$$(\nabla \cdot \mathbf{v})_i = \sum_{j=1}^{N} \frac{m_j}{\rho_{ij}} (\mathbf{v}_j - \mathbf{v}_i) \cdot \nabla_i W_{ij}, \tag{15}$$

respectively, where $\rho_{ij} = (\rho_i + \rho_j)/2$. A form similar to Eq. (14) is used to evaluate the temperature gradient for the heat flux in Eq. (5).

The SPH representation of the Korteweg tensor (6) involves the approximation of second-order derivatives of the density. A similar problem arises when trying to solve the heat conduction equation in cosmological applications [37]. In particular, the presence of second derivatives makes the standard SPH kernel interpolation to be noisy and quite sensitive to particle disorder, which, in turn, can lead to an unstable time integration if large local gradients arise due to noise [38]. Here we use a method where the SPH representation of the Laplace operator involves only first-order derivatives of the smoothing kernel via a Taylor series expansion of the density field [37,38], which has been generalized for the approximation of mixed derivatives by Yildiz *et al.* [39]. We start by rewriting Eq. (6) in the form

$$\mathbb{K} = \frac{K}{2} \left(\rho\nabla^2\rho + \frac{1}{2}\nabla^2\rho^2\right)\mathbb{I} - K\nabla\rho\nabla\rho, \tag{16}$$

which in Cartesian coordinates involves operator terms like $\partial^2/\partial x^2$, $\partial^2/\partial y^2$, and $\partial^2/\partial x\partial y$. Following the three-dimensional procedure outlined in Ref. [39], we can derive a stable kernel approximation in two dimensions for the second

spatial derivative as follows:

$$\frac{\partial^2\rho_i}{\partial x_i^k\partial x_i^l}=\int\frac{(\rho_j-\rho_i)}{|\mathbf{x}_{ij}|}\left(\frac{4x_{ij}^kx_{ij}^l}{|\mathbf{x}_{ij}|^2}-\delta^{kl}\right)\frac{x_{ij}^l}{|\mathbf{x}_{ij}|}\frac{\partial W_{ij}}{\partial x_i^l}d^2\mathbf{x}_j, \tag{17}$$

where the integration is taken over the whole plane, $\mathbf{x}_{ij}=\mathbf{x}_i-\mathbf{x}_j$, δ^{kl} is the delta Kronecker, and k and l are coordinate indices equal to 1 or 2 such that $x^1=x$ and $x^2=y$ in Cartesian coordinates. Contracting on indices k and l (with $k=l$), the above expression produces the SPH Laplacian approximation

$$(\nabla^2\rho)_i=2\sum_{j=1}^N\frac{m_j}{\rho_j}\frac{(\rho_j-\rho_i)}{|\mathbf{x}_{ij}|^2}\mathbf{x}_{ij}\cdot\nabla_iW_{ij}, \tag{18}$$

while for $k\neq l$ we obtain the SPH approximation of the mixed derivative

$$\left(\frac{\partial^2\rho}{\partial x\partial y}\right)_i=4\sum_{j=1}^N\frac{m_j}{\rho_j}\frac{(\rho_j-\rho_i)}{|\mathbf{x}_{ij}|^2}\frac{x_{ij}y_{ij}}{|\mathbf{x}_{ij}|^2}\mathbf{x}_{ij}\cdot\nabla_iW_{ij}. \tag{19}$$

The SPH representations (18) and (19) are much less sensitive to particle disorder than the corresponding direct ones, which use the second derivative of the kernel [40]. Alternative representations for the second derivatives which improve the accuracy of standard SPH were reported by Zhou *et al.* [41].

We write Eqs. (11) and (12) in Cartesian coordinates so that $\mathbf{v}=(v_x,v_y)$, $\mathbf{q}=(q_x,q_y)$, only the xx, xy, and yy components of the stress tensors $\mathbb{T}$ and $\mathbb{K}$ are retained, and all field variables are functions of the (x,y) coordinates and time t. Using the SPH approximations (18) and (19), and expressing the product $\nabla\rho\nabla\rho$ in Eq. (16) in terms of only second derivatives of ρ, the components of the Korteweg tensor entering the SPH momentum Eq. (11) can be written as follows

$$\mathcal{K}_i^{xx}=\frac{K}{2}\sum_{j=1}^Nm_j\frac{\left(\rho_j+2\rho_i-3\rho_i^2/\rho_j\right)}{|\mathbf{x}_{ij}|^2}\mathbf{x}_{ij}\cdot\nabla_iW_{ij}$$
$$-K\sum_{j=1}^N\frac{m_j}{\rho_j}\frac{(\rho_j-\rho_i)^2}{|\mathbf{x}_{ij}|^2}x_{ij}\frac{\partial W_{ij}}{\partial x_i}, \tag{20}$$

$$\mathcal{K}_i^{yy}=\frac{K}{2}\sum_{j=1}^Nm_j\frac{\left(\rho_j+2\rho_i-3\rho_i^2/\rho_j\right)}{|\mathbf{x}_{ij}|^2}\mathbf{x}_{ij}\cdot\nabla_iW_{ij}$$
$$-K\sum_{j=1}^N\frac{m_j}{\rho_j}\frac{(\rho_j-\rho_i)^2}{|\mathbf{x}_{ij}|^2}y_{ij}\frac{\partial W_{ij}}{\partial y_i}, \tag{21}$$

$$\mathcal{K}_i^{xy}=-2K\sum_{j=1}^N\frac{m_j}{\rho_j}\frac{(\rho_j-\rho_i)^2}{|\mathbf{x}_{ij}|^2}\frac{x_{ij}y_{ij}}{|\mathbf{x}_{ij}|^2}\mathbf{x}_{ij}\cdot\nabla_iW_{ij}, \tag{22}$$

where $\mathcal{K}^{xy}=\mathcal{K}^{yx}$ and the superscript H has been omitted for simplicity.

It has been shown that the stability and accuracy of SPH is significantly improved when the smoothing length is allowed to vary adaptively using a density kernel estimation [32]. Here we adopt a variant of the method where the density is first estimated using Eq. (10) with $h=h_{i,0}$ (the value of h at $t=0$) and the particle distribution at the beginning of each time step ($t=t^n$). These values are then used to calculate local bandwidth factors λ_i for each particle according to

$$\lambda_i=k\left(\frac{\rho_i}{\bar{g}}\right)^{-\epsilon}, \tag{23}$$

where k is a constant of order unity, ϵ is the sensitivity parameter with $0\leqslant\epsilon\leqslant1$, and $\bar{g}$ is the geometric mean of the density estimates given by

$$\log\bar{g}=\frac{1}{N_{\rm tot}}\sum_{i=1}^{N_{\rm tot}}\log\rho_i, \tag{24}$$

where the sum is taken over all particles in the computational domain. Adaptive values of the smoothing lengths are then defined as $h_i^{n+1}=\lambda_ih_{i,0}$. The adaptive estimator step then consists of recalculating the density field using Eq. (10) with $h_i=h_i^{n+1}$. This approach involves two free parameters, namely k and ϵ. While k is of order unity, the optimal choice of ϵ is problem dependent and is determined from stability considerations [32,33]. The application of the method to the formation of equilibrium vdW drops confirmed the predictions of a linear stability analysis with optimum values of ϵ lying in the range between 0.5 and 0.8 [32]. When ϵ was allowed to vary within this range no symptoms of the tensile instability were apparent in the form of ringlike clustering or binary pairs of particles. To improve the conservation of the angular momentum and total energy, the actual calculations were carried out by enforcing the symmetrization of the kernel estimate with respect to particle pairs by replacing h_i in the kernel function by the mean $h_{ij}=(h_i+h_j)/2$. In this work, the quartic spline kernel of Lucy [42] is employed as the smoothing interpolant W_{ij} so that only particles within a radius equal to the local smoothing length will contribute to the SPH summations. A velocity Verlet time integration method coupled to a predictor-corrector scheme is employed to advance the field variables from $t=t^n$ to $t=t^{n+1}$ with a constant time step $\Delta t=0.005$.

IV. NUMERICAL RESULTS

Circular drops floating in a vapor atmosphere are obtained by starting the calculations from a square-shaped liquid, consisting of 900 SPH particles of equal mass ($m_i=m$) regularly distributed in a square-cell array. The particles are initially at rest and separated by a dimensionless distance $\Delta x=\Delta y=0.78$. As in Refs. [22,31] we use reduced units and set $\bar{k}_B=1$, $\bar{\alpha}=2$, and $\bar{\beta}=0.5$. In these units the critical point is specified by $\rho_c=2/3$, $p_c=8/27$, and $T_c=32/27\approx1.19$. For this vdW fluid the sound speed is given by

$$c_s=\left(\frac{\bar{k}_BT}{(1-\bar{\beta}\rho)^2}-2\bar{\alpha}\rho\right)^{1/2}, \tag{25}$$

so that the initial density and temperature must satisfy the constraints $\rho_0<1/\bar{\beta}$ and $\bar{k}_BT_0>2\bar{\alpha}\rho(1-\bar{\beta}\rho)^2$ for thermodynamic stability. In reduced units the shear and bulk viscosities are taken to be $\eta=1$ and $\zeta=0.1$, while the thermal conductivity is set to $\kappa=5$. A value of κ this large produces a fast temperature adjustment and reduces density fluctuations in the drop. For most calculations, the gradient energy coefficient is chosen to be $K=0.1$. A separate set of calculations was

carried out with $K = 1$ to quantify the effects of increasing the strength of the Korteweg force. Following Sigalotti and López [32], we set $k = 0.9$ and $\epsilon = 0.6$ for the adaptive kernel estimation parameters in Eq. (23).

The square-shaped liquid is confined within a box of sides $L = 60$, where periodic boundary conditions are applied so that vapor particles exiting the box on one side are allowed to enter the opposite side. Initially the smoothing lengths are $h_{i,0} = 4\Delta x$ and $H_{i,0} = 2h_{i,0}$. Owing to the adaptive kernel estimation, smaller values of $h_{i,0}$ and $H_{i,0}$ were seen to produce essentially the same results. Figure 1(a) shows the temperature-density (T-ρ) phase diagram for a vdW fluid. The symbols on the plot mark the position on the phase diagram of the initial density and temperature for all models. For a given initial density, five separate sequences of model calculations are presented for varying initial temperatures. The initial density for each sequence is varied by varying the mass of the particles in the range $0.4 \leqslant m \leqslant 1$, while keeping all other parameters the same. The area below the spinodal line (dashed line) is the (mechanically) unstable region, where $(\partial p/\partial \rho)_T < 0$ and the fluid separates spontaneously into two phases due to spinodal decomposition. Outside this there is a region of metastable (i.e., mechanically stable but thermodynamically unstable) states bounded by the binodal line (solid line), which is determined by the condition that the Gibbs free energy is the same in both phases. Below this line where $T < T_c$, the isotherms of the vdW equation wiggle with the pressure achieving a minimum and then a maximum with increasing volume (vdW loop). While these two extrema lie on the spinodal curve, the intersections of a given isotherm with the binodal curve through the loop define a horizontal line such that the areas enclosed by this line and the spinodal pressures are equal (Maxwell's construction). The horizontal line fixes the coexistence pressure. Its intersections with the binodal correspond to states of minimum free energy and define the equilibrium volumes of liquid-vapor coexistence at different temperatures.

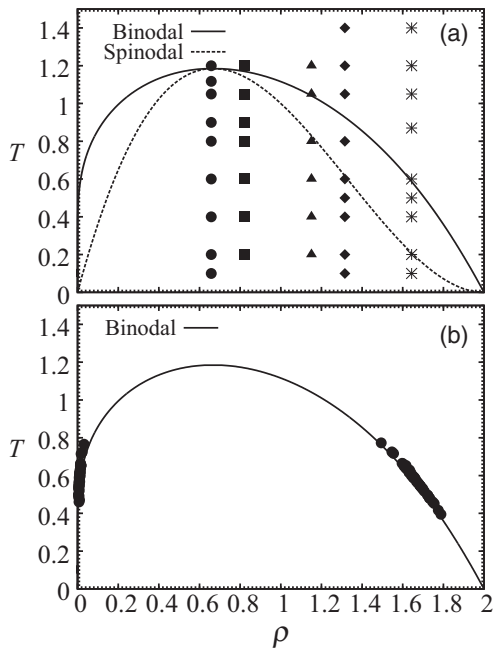

FIG. 1. (a) Phase diagram showing the theoretically calculated binodal and spinodal curves for a van der Waals fluid. The overlayed symbols denote the initial state of the models. The initial density is varied by varying the mass of the particles: $m = 0.4$ (dots), 0.5 (squares), 0.7 (triangles), 0.8 (diamonds), and 1 (asterisks). (b) Densities and temperatures of the coexisting phases as obtained from the numerical simulations (dots) compared to the binodal curve for a vdW fluid (solid line).

A. Liquid-vapor decomposition of vdW drops

To validate the numerical model, Fig. 1(b) compares the equilibrium densities and temperatures of the liquid and gas phases as obtained from the numerical simulations with the binodal curve as calculated using the Maxwell's equal-area construction. The filled dots are the SPH results, which refer to average particle densities and temperatures within a small circle about the drop center for the liquid phase and over a thin ring far away from the drop for the vapor phase. The SPH results are seen to match the theoretical predictions very well. Dots deviating slightly from the binodal correspond to a few models starting with temperatures inside the miscibility gap close to the critical point. In these cases, equilibrium is not being fully reached within the simulation time. Drops with $T_0 < 0.6$ and $0.661 \leqslant \rho_0 \leqslant 1.322$ (corresponding to particle masses in the range $0.4 \leqslant m \leqslant 0.8$) undergo spinodal decomposition and achieve equilibrium states with temperatures higher than the initial values, while for $T_0 > 0.6$ the converse occurs and equilibrium is reached at temperatures lower than the initial ones. As expected, models with initial conditions close to the liquid zone of the phase diagram, i.e., with $T_0 \leqslant 0.3$ and $\rho_0 \approx 1.652$ (for $m = 1$) [see Fig. 1(a)], condensed into equilibrium liquid drops with no vapor phase, while for $T_0 > 0.3$ stable liquid drops with a very sparse vapor atmosphere are formed.

Final drop configurations are shown in Fig. 2 for different equilibrium temperatures below T_c. The panels display the particle positions (middle column) and a smoothed representation of the density using the visualization tool SPLASH for SPH simulations [43] (right column). The plots on the left column are the corresponding rendered mass density field overlayed on the phase diagram, showing the normalized distribution of particle densities. From top to bottom a sequence of four equilibrated drops is displayed for increasing equilibrium temperatures and decreasing equilibrium liquid densities. The first row of panels depicts an equilibrium drop with $\rho_l \approx 1.75$ and $T \approx 0.46$ surrounded by a very sparse vapor. For this model $m = 1$ and since $\alpha = \bar{\alpha} m^2 = 2m^2$, the molecular attraction in the liquid is stronger and so only a few molecules escape the intermolecular forces and enter the vapor phase. As the particle mass is lowered, the strength of the intermolecular forces is also reduced. Therefore during spinodal decomposition a greater number of molecules is allowed to enter the vapor region and the evolution ends up with progressively smaller liquid drops and denser vapor atmospheres as shown in the remaining panels of Fig. 2.

The radial variations of the density, pressure, and temperature across the system are shown in Figs. 3 and 4 for two of the equilibrium drops depicted in Fig. 2, i.e., at coexistence temperatures $T \approx 0.64$ ($m = 0.8$) and ≈ 0.66 ($m = 0.5$),

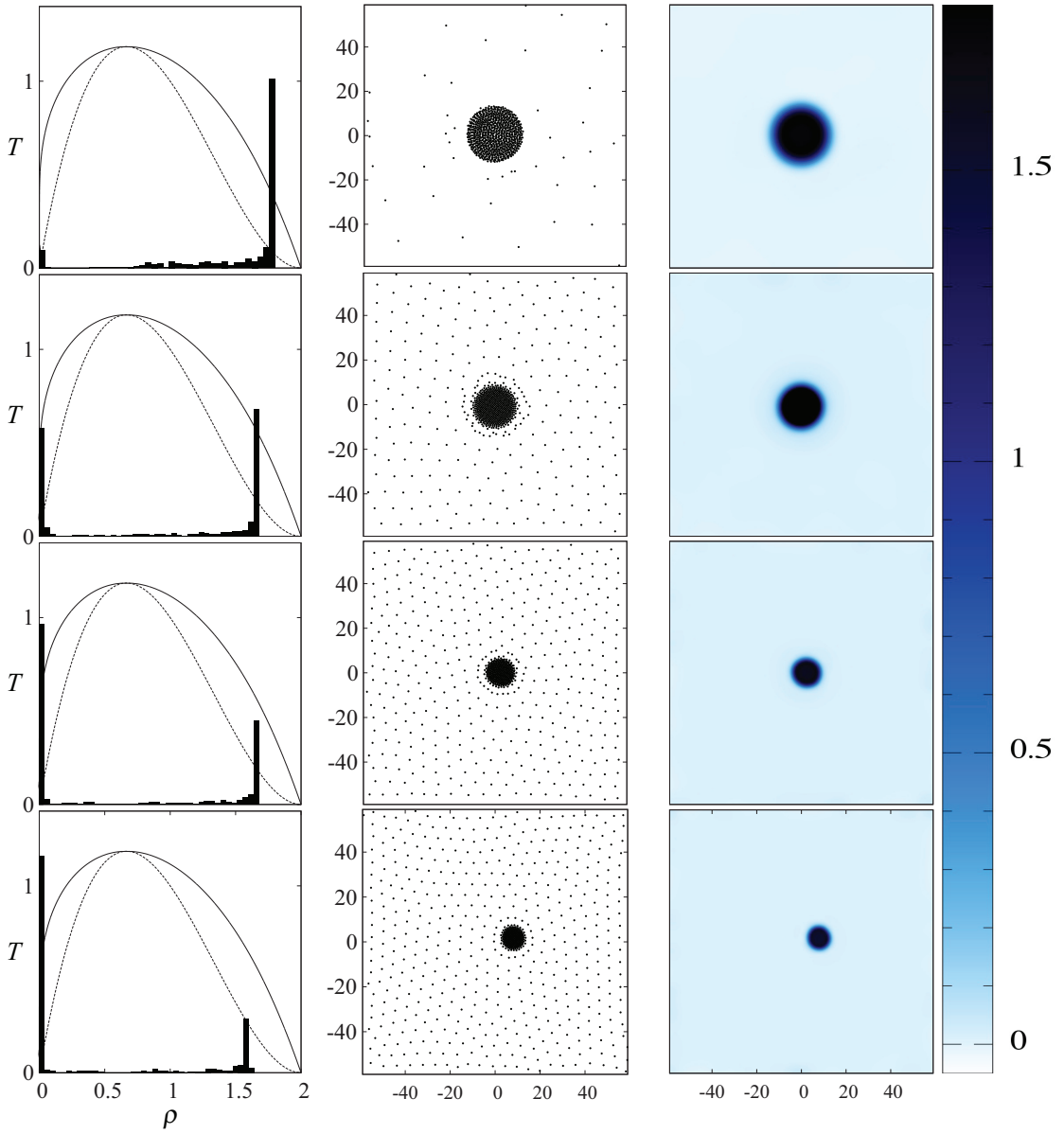

FIG. 2. (Color) Stable liquid drops in a vapor atmosphere. The liquid and the vapor phases are in thermal equilibrium with coexistence temperatures from top to bottom of ≈ 0.46, 0.64, 0.66, and 0.75. The plots show the normalized distribution of SPH particle densities overlayed on the phase diagram (left), the particle positions showing the liquid drop and ambient vapor (middle), and the spatially rendered mass density field using the visualization tool SPLASH (right). The color-scale bar and numbers on the right border indicate the density contrast in terms of our reduced units.

respectively. The spherically symmetric profiles are obtained by dividing the entire system into thin concentric circular shells so that the value of a quantity at a radius r from the drop center of mass corresponds to an average over the particles within the shell centered at that radius. In Fig. 4 the profiles are compared for two different choices of the gradient energy coefficient K in Eq. (15). The vertical line in the density plots mark the position of the equimolar radius (see next section). The results are qualitatively similar to those of Nugent and Posch [22] for a drop with $T \approx 0.91$ (their Figs. 2, 3, and 4). Here the use of an adaptive density kernel estimation reduces the size of the errors carried by Eq. (10) due to particle inconsistency at the borders of the liquid drop, resulting in much less smooth density profiles there from the beginning, and controls the amount of smoothing that is effectively applied in the vapor phase. This is so because this class of estimates requires a less broad kernel than the fixed kernel approach in zones where the density is low. This later aspect results in better spatial resolution across the liquid-to-vapor transition zone and therefore in more rapid density fall-offs through the interface than in the calculations of Nugent and Posch [22], where the width of the kernel is kept fixed during the evolution. We note from Fig. 4 that increasing K from 0.1 to 1 causes little differences in the final equilibrium profiles as all curves essentially overlap, with the exception of the temperature variation where $K = 1$ results in slightly higher temperatures in the bulk phases.

We see from Figs. 3 and 4 that moving from the drop center to the interface the liquid overheats and the pressure

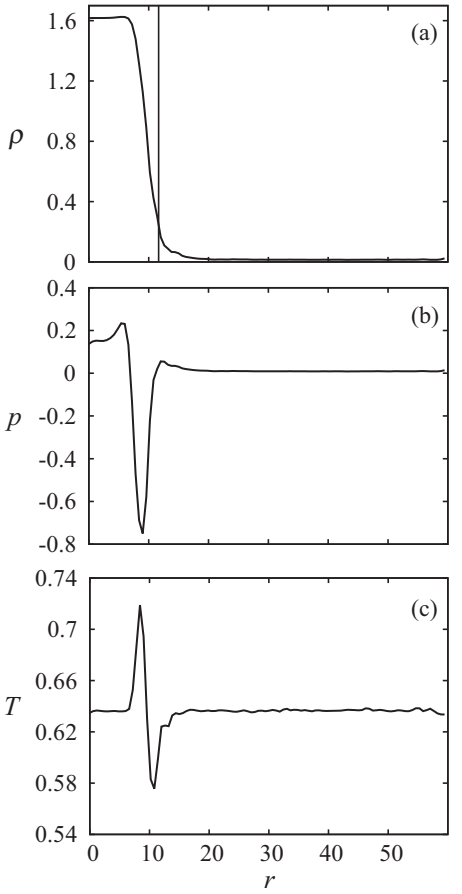

FIG. 3. (a) SPH-averaged radial density, (b) pressure, and (c) temperature profiles for an equilibrium drop with a temperature $T \approx 0.64$. The vertical line in (a) marks the position of the equimolar radius. All quantities are expressed in terms of our reduced units.

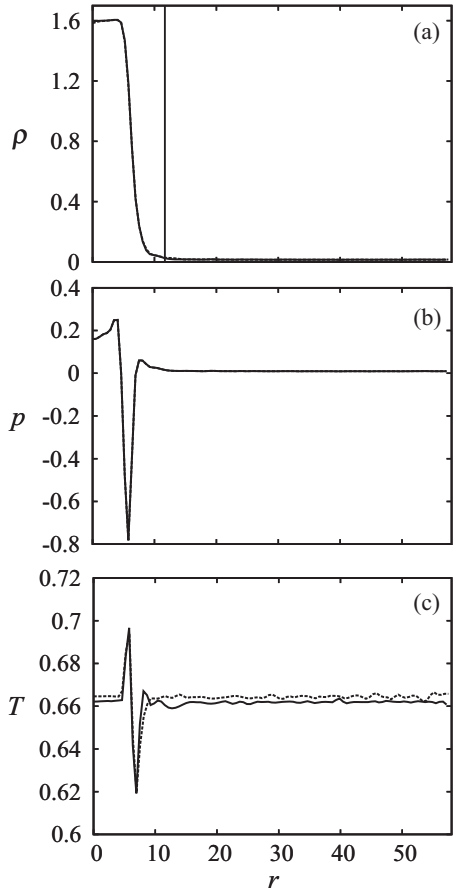

FIG. 4. (a) SPH-averaged radial density, (b) pressure, and (c) temperature profiles for an equilibrium drop with a temperature $T \approx 0.66$. The profiles obtained with $K = 0.1$ (solid lines) are compared to those calculated using $K = 1$ (dashed line) for an identical model. The vertical line in (a) marks the position of the equimolar radius. All quantities are expressed in terms of reduced units.

variations become negative with respect to the coexistence pressure (Maxwell's tie line). This is followed by a region of undercooled vapor with positive pressure differences before entering the vapor phase. The first extreme is a stability limit for the liquid state, where the liquid overheats without vaporizing, while the second one is the stability limit for the vapor state, where the vapor undercools without condensing. Away from these extrema, the temperature at the drop center and in the vapor atmosphere are nearly the same, indicating that the drop is very close to thermal equilibrium. The vdW loop is evident from the variation of the pressure through the interface. In real systems other stability limits exist, such as for melting and crystallization [44], which, however, cannot be modeled with a vdW equation of state.

B. Surface tension

Although the vdW mean-field theory has been successful in capturing both the liquid and vapor states of matter, as well as predicting the coexistence region by using the Maxwell construction, the surface properties of the vdW model can be predicted only in an approximate sense. In general, knowledge of either the density gradient or the radial density distribution through the liquid-vapor interface is required to determine the surface tension [1]. However, this information cannot be obtained experimentally for the vdW model because it represents only an approximation to real fluids [23].

The surface tension of the circular drops can be easily calculated using the Young-Laplace equation

$$p_l - p_v = \frac{2\sigma}{R}, \tag{26}$$

where p_l is the pressure in the interior of the drop, here calculated as the average particle pressure within a small circle around the center of the drop, p_v is the pressure in the ambient vapor, corresponding to an average value taken over a thin ring far away from the drop, and R is the radius of the equimolar surface, which separates the liquid from the vapor. The Tolman length correcting for the deviations of the surface tension from its planar value in Eq. (26) is not considered here because for almost all models it was smaller than the simulation error bars. In two dimensions, the equimolar radius can be defined as [1]

$$R^2 = -\frac{1}{\rho_l - \rho_v} \int_0^\infty r^2 \frac{d\rho}{dr} dr, \tag{27}$$

where $d\rho/dr$ is the radially symmetric variation of the density.

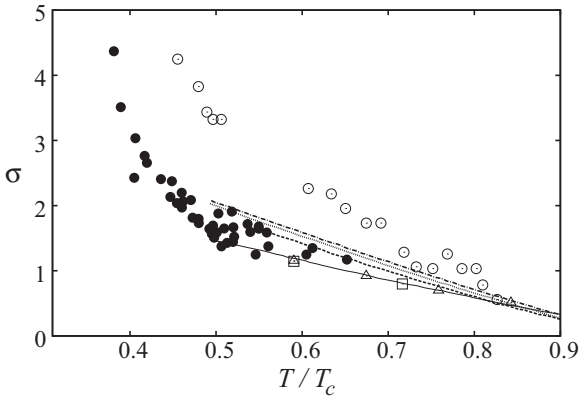

FIG. 5. Dependence of the surface tension σ on temperature for the vdW drops. The SPH results (filled dots) are compared with those of Nugent and Posch [22] (open dots). The open triangles and open squares refer to molecular dynamics [45] and Monte Carlo simulations [46] for a Lennard-Jones fluid, respectively, while the continuous lines correspond to available experimental data for liquid argon [47] (solid line), kripton (dashed line), ethane (dotted line), and R152a (dot-dashed line) [48].

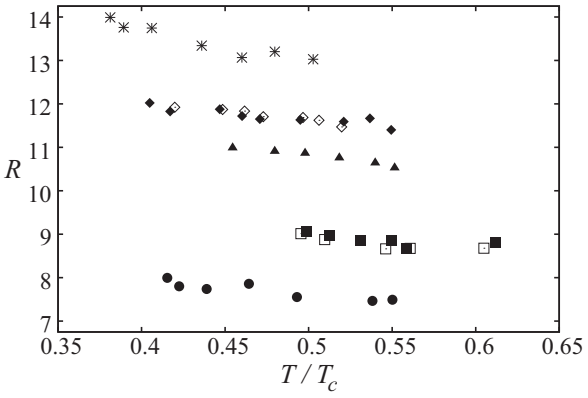

FIG. 6. Dependence of the equimolar radius R on temperature. The same symbols in Fig. 1(a) are used to identify the initial state for each sequence of data. The squares and diamonds represent models with $m = 0.5$ and 0.8, respectively, for $K = 0.1$ (filled symbols) and $K = 1$ (open symbols).

The temperature dependence of the surface tension is depicted in Fig. 5 for all drops. The estimated accuracy of the data is always less than $\pm 15\%$. We compare our results to those from the SPH simulations of Nugent and Posch [22] (open circles). Although their results follow a qualitatively similar trend to those predicted here, they are comparatively higher. This difference can be attributed to a better treatment of the diffuse interface in the present work. Molecular dynamics [45] (open squares) and Monte Carlo simulations [46] (open triangles) taking the effects of two-body interactions in a Lennard-Jones fluid close to phase coexistence are also included in Fig. 5 along with experimental data for liquid argon [47], krypton, ethane, and the refrigerant R152a [48], which are all represented by continuous lines. Our results can be compared to those from molecular dynamics and Monte Carlo simulations in the range of temperatures between $T/T_c \approx 0.6$ and 0.7, for which good agreement is observed. A comparison to the experimental data shows a reasonably good agreement between our SPH simulations and the experiment.

The variation of the equimolar radius with temperature is shown in Fig. 6. The same symbols of Fig. 1(a) are used to represent the data in this and subsequent figures to identify the initial conditions to which the data belong. We see that square-shaped liquids of higher initial density produced equilibrated drops of larger sizes, higher liquid densities, and lower vapor densities at phase coexistence for a fixed initial temperature. This occurs because in the present models the initial liquid density is decreased by reducing the mass of the particles, which is equivalent to decrease the strength (α) of the attractive forces in the vdW equation of state (7). For all sequences the equimolar radius decreases as the equilibrium temperature increases. This trend is consistent with the surface tension vanishing as the critical temperature is approached, which according to Eq. (26) implies that $R \to 0$ at the critical point.

C. Vapor pressure

It is well known that the quantity of vapor above a liquid increases with the temperature and is normally measured as the vapor pressure of the system. As the temperature increases, a greater number of molecules have enough energy to escape the intermolecular attraction forces of the liquid and enter the vapor phase, thereby increasing the vapor pressure. Therefore, a measure of the molecular attraction of the liquid is the latent heat (or enthalpy) of vaporization $\Delta H_{\rm vap}$, which is the energy required to transform a certain quantity of liquid into vapor without a change in temperature. In this way, large values of $\Delta H_{\rm vap}$ would indicate strong attractive forces between the liquid's molecules. A mathematical relation between the vapor pressure and the temperature is provided by the well known Clausius-Clapeyron equation

$$p_v = A \exp\left(-\frac{\Delta H_{\rm vap}}{\bar{k}_B T}\right), \tag{28}$$

where A is an experimental constant related to the normal boiling point and $\bar{k}_B = 1$. If we take the natural logarithm on both sides of the above equation, we find that

$$\ln p_v = -\frac{\Delta H_{\rm vap}}{\bar{k}_B}\frac{1}{T} + C, \tag{29}$$

which is the equation of a straight line of slope equal to $-\Delta H_{\rm vap}/\bar{k}_B$. Figure 7 depicts $\ln p_v$ as a function of the inverse of the temperature for all drops. The solid straight line gives the best fit of the data to Eq. (29) and has a slope $\Delta H_{\rm vap}/\bar{k}_B \approx 2.08$, which is very close to $\bar{\alpha} = 2$. However, we note that at the right bottom of the figure the data points represented by asterisks and diamonds are randomly scattered and deviate substantially from the linearly arranged distribution observed for all other data points. This occurs because these models evolved from initial conditions very close to the liquid zone of the phase diagram [see Fig. 1(a)], forming stable liquid drops with essentially no vapor atmosphere as shown in the top panels of Fig. 2. In addition, the filled dots in the left top of the figure, corresponding to models with $m = 4$ and initially close to the critical point, also deviate from the general

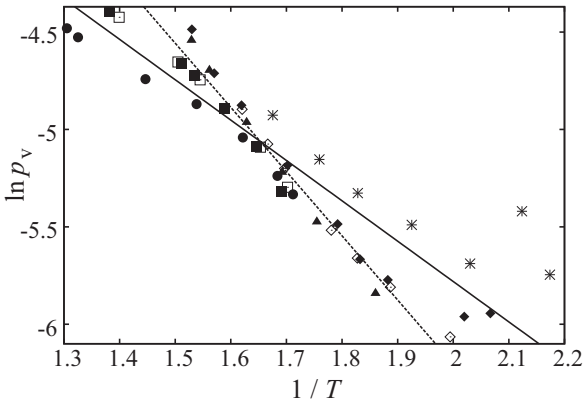

FIG. 7. Natural logarithm of the vapor pressure as a function of the inverse of the temperature for all models. The same symbols in Fig. 1(a) are used to identify the initial state for each sequence of data. The solid line fits the numerical data to the Clausius-Clapeyron equation (29) and the dashed line fits the same data by excluding the scattered points, corresponding to liquid drops with essentially no vapor atmosphere or not fully in equilibrium. The slope of the former linear fit is $\Delta H_{\rm vap}/\bar{k}_B \approx 2.08$, while that of the latter is $\Delta H_{\rm vap}/\bar{k}_B \approx 3.4$, which gives a better representation of the numerical data and defines the vaporization pressure in reduced units for this vdW fluid.

trend because they never reached full equilibrium within the simulation time. If we discard these points, the best linear fit to the remaining data is depicted by the dashed line in Fig. 7 and has a slope $\Delta H_{\rm vap}/\bar{k}_B \approx 3.4$, which is more representative of the constant value of the enthalpy of vaporization for this vdW fluid. For comparison, Fig. 8 plots the dependence of the vapor pressure on temperature. The solid line represents the best exponential fit to all data and obeys the relation $p_v \approx 0.19\exp(-2.10/T)$, implying that $\Delta H_{\rm vap}/\bar{k}_B \approx 2.10$, while the dashed line represents the best exponential fit by excluding the scattered data and corresponds to the relation

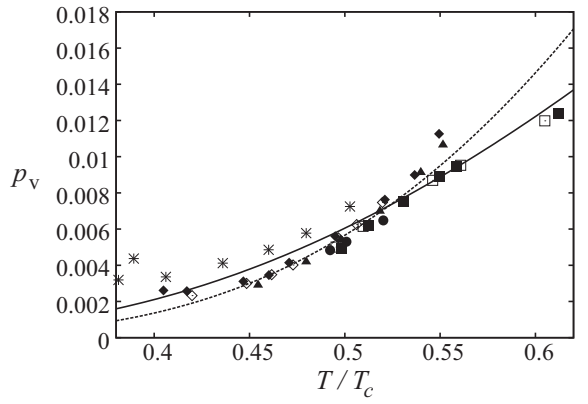

FIG. 8. Dependence of the vapor pressure p_v on temperature for all models. The solid line represents the best exponential fit to all numerical data: $p_v \approx 0.19\exp(-2.10/T)$, yielding $\Delta H_{\rm vap}/\bar{k}_B \approx 2.10$. The dashed line represents the same fit when the scattered data, corresponding to liquid drops with essentially no vapor atmosphere or not fully in equilibrium, are omitted. It satisfies the relation $p_v \approx 1.69\exp(-3.42/T)$ and provides a better representation of the Clausius-Clapeyron relation for the 2D vdW drops.

$p_v \approx 1.69\exp(-3.42/T)$, which again gives a much better representation of the Clausius-Clapeyron relation for these low and moderate vapor pressures.

We remind that several approximations are necessary to write the Clausius-Clapeyron relation in the form given by Eqs. (28) and (29). First, the enthalpy of vaporization $\Delta H_{\rm vap}$ is assumed to be constant over the temperature range of interest, while the vapor is assumed to be an ideal gas. Although these two approximations are good at low and moderate pressures for most substances, they fail at high pressures and near the critical point. Under these conditions, Eqs. (28) and (29) will give inaccurate results. Second, the change in volume that accompanies evaporation (or sublimation) is assumed to be equal to the volume of the vapor produced and the external pressure is supposed to have no effect on the vapor.

The slopes of the linear fits in Fig. 7 are determined by the ratio of latent heat released in the phase transition and the discontinuity between the liquid and vapor volumes. Since the entropy, expressed as the first derivative of the Helmholtz potential with respect to temperature, and the volume, expressed as the first derivative of the Gibbs free energy with respect to pressure, are both discontinuous across the line, the Clausius-Clapeyron equation applies to first-order phase transitions. As we approach the limit $T/T_c \to 1$, the discontinuity diminishes and the liquid entropy tends to the gas entropy. At $T/T_c = 1$ the liquid cannot be distinguished from the gas since, in addition, their molar volumes and heat capacities at constant volume become the same. So, at the critical temperature we have a second-order phase transition. Furthermore, as $T/T_c \to 1$, the enthalpy of vaporization becomes temperature dependent [49], i.e.,

$$\frac{\Delta H_{\rm vap}}{T} \propto \left(1 - \frac{T}{T_c}\right)^{1/2}, \tag{30}$$

so that $\Delta H_{\rm vap} \to 0$ as $T/T_c \to 1$. On the other hand, in the limit of low temperatures, when $T/T_c \to 0$, the enthalpy of vaporization becomes independent of temperature and approaches the finite limit $\Delta H_{\rm vap} = \bar{\alpha}/\bar{\beta}$ [49]. Since $\bar{\alpha} = 2$ and $\bar{\beta} = 0.5$ for our vdW fluid, this limit gives $\Delta H_{\rm vap} = 4$. This exact value differs from the slope of the dashed straight line in Fig. 7 by ∼15% and from that of the solid line by a factor of 2, implying that the former is a much better representation of the Clausius-Clapeyron relation. The same is true for the dashed curve in Fig. 8. Although the limit when $T/T_c \to 0$ may be a useful test to check the reliability of the numerical results for this vdW models, it is interesting only from a theoretical point of view because for real substances there are no liquid-vapor phase transitions at $T \to 0$, and so the near-zero temperature limit should be applied in the temperature interval $T_{\rm tp} < T \ll T_c$, where $T_{\rm tp}$ is the triple-point temperature. We conclude that the Clausius-Clapeyron relation is very well reproduced by the numerical calculations in the range of moderately low vapor pressures where the enthalpy of vaporization is expected to be approximately constant.

V. CONCLUSION

In this paper we have applied the method of smoothed particle hydrodynamics (SPH) to model liquid-vapor phase separation in nonisothermal, van der Waals (vdW) liquid drops

initially in a nonequilibrium state for a range of densities and temperatures. To model the rapid but smooth transition across the liquid-vapor interface as a diffuse region and the effects of surface tension properly we have relied on the diffuse-interface model, where convective motion at the late stages of phase separation is accounted for by means of a reversible, nonequilibrium (Korteweg) force entering the momentum equations [25]. An adaptive density kernel estimation procedure was implemented into the SPH scheme to resolve high- and low-density regions in the flow simultaneously and with a minimum amount of smoothing, using the particle density distribution. This procedure requires less broad kernels in regions where the density is low compared to a fixed kernel approach and other conventional adaptive SPH schemes. It therefore results in a reduction of the rates of numerical dissipation and diffusion, thereby improving the stability and accuracy of SPH [32,33].

The models all start from a square-shaped liquid and stable circular drops floating in its vapor atmosphere are formed by spinodal decomposition for a wide range of the initial conditions. The densities and temperatures of the coexisting liquid and vapor are found to closely match the binodal curve as predicted by the vdW equation of state. At subcritical temperatures, the pressure excess at the center of an equilibrated drop gives rise to the surface tension. Since extracting the surface tension from the slope of the density variation at the equimolar radius, where the liquid phase separates from the vapor, is difficult [1], we calculate it directly from the Young-Laplace equation. Although our results predict a dependence of the surface tension on temperature which is qualitatively similar to that calculated by Nugent and Posch [22], their values are higher at comparable temperatures. We attribute this discrepancy to differences in the interface treatment in both sets of SPH calculations. A comparison to experimental data and the results of molecular dynamics [45] and Monte Carlo simulations [46] for a Lennard-Jones fluid close to coexistence shows a much better agreement with our SPH predictions for the surface tension. On the other hand, the Clausius-Clapeyron equation, which characterizes the discontinuous liquid-to-vapor phase transition, is very well reproduced by the numerical dependence of the vapor pressure on temperature, yielding an estimate of the vaporization pressure for this vdW fluid.

ACKNOWLEDGMENTS

One of us (J.K.) acknowledges the Consejo Nacional de Ciencia y Tecnología of Mexico (CONACyT) for partial support under Project No. CONACyT-EDOMEX-2011-C01-165873. We thank the anonymous referees for a list of valuable suggestions and recommendations.

[1] J. S. Rowlinson and B. Widom, *Molecular Theory of Capillarity* (Dover, New York, 2002).
[2] E. P. Favvas and A. Ch. Mitropoulos, J. Eng. Sci. Tech. Rev. **1**, 25 (2008).
[3] J. W. Cahn, Trans. Metall. Soc. AIME **242**, 166 (1968).
[4] J. E. Hilliard, in *Phase Transformations*, edited by H. I. Aaronson (American Society for Metals, Metals Park, OH, 1970), pp. 497–560.
[5] D. D. Fontaine, in *Solid State Physics*, Vol. 34, edited by H. Ehrenreich, F. Seitz, and D. Turnbull (Elsevier, Amsterdam, 1979), pp. 73–274.
[6] K. V. Chuistov, *Aging of Metallic Alloys* (Naukova Dumka, Kiev, 1985) (in Russian).
[7] B. Ditchek and L. H. Schwartz, Ann. Rev. Mater. Sci. **9**, 219 (1979).
[8] W. R. Cribb and J. O. Ratka, Adv. Mater. Proc. **160**(11), 27 (2002).
[9] A. Putnis, *Introduction to Mineral Sciences* (Cambridge University Press, Cambridge, England, 1992).
[10] P. Papon, J. Leblond, and P. H. E. Meijer, *The Physics of Phase Transitions; Concepts and Applications* (Springer-Verlag, Berlin, 2002).
[11] M. U. Kim, J. P. Ahn, H. K. Seok, E. Fleury, H. J. Chang, D. H. Kim, P. R. Cha, and Y. C. Kim, Met. Mater. Int. **15**, 193 (2009).
[12] J. W. Cahn and J. E. Hilliard, J. Chem. Phys. **31**, 688 (1959).
[13] J. W. Cahn, Acta Metall. **9**, 795 (1961).
[14] Y. Guissani and B. Guillot, J. Chem. Phys. **98**, 8221 (1993).
[15] W. R. Osborn, E. Orlandini, M. R. Swift, J. M. Yeomans, and J. R. Banavar, Phys. Rev. Lett. **75**, 4031 (1995).
[16] B. T. Nadiga and S. Zaleski, Eur. J. Mech. B, Fluids **15**, 885 (1996).
[17] V. Sofonea, A. Lamura, G. Gonnella, and A. Cristea, Phys. Rev. E **70**, 046702 (2004).
[18] R. Borcia and M. Bestehorn, Phys. Rev. E **75**, 056309 (2007).
[19] A. Charles and P. Daivis, in *Proceedings of the 18th World IMACS Congress and MODSIM09 International Congress of Modelling and Simulation*, edited by R. S. Anderssen, R. D. Braddock, and L. T. H. Newham (The Modelling and Simulation Society of Australia and New Zealand Inc. and The International Association for Mathematics and Computers Simulation, Canberra, Australia, 2009), pp. 303-309.
[20] A. G. Lamorgese and R. Mauri, Phys. Fluids **21**, 044107 (2009).
[21] D. Reith, K. Bucior, L. Yelash, P. Virnau, and K. Binder, J. Phys: Condensed Matter **24**, 115102 (2012).
[22] S. Nugent and H. A. Posch, Phys. Rev. E **62**, 4968 (2000).
[23] N. G. Hadjiconstantinou, A. L. Garcia, and B. J. Alder, Physica A **281**, 337 (2000).
[24] P. B. Warren, Phys. Rev. E **68**, 066702 (2003).
[25] D. M. Anderson, G. B. McFadden, and A. A. Wheeler, Annu. Rev. Fluid Mech. **30**, 139 (1998).
[26] D. Jasnow and J. V. Nals, Phys. Fluids **8**, 660 (1996).
[27] D. Jacqmin, J. Fluid Mech. **402**, 57 (2000).
[28] D. J. Korteweg, Arch. Néerl. Sci. Exactes Nat. Sér. II, Tome **6**, 1 (1901).
[29] J. D. van der Waals, J. Stat. Phys. **20**, 200 (1979).
[30] B. W. Silverman, *Density Estimation for Statistics and Data Analysis* (Chapman & Hall, London, 1996).

[31] H. López and L. D. G. Sigalotti, Phys. Rev. E **73**, 051201 (2006).
[32] L. D. G. Sigalotti and H. López, Comput. Math. Appl. **55**, 23 (2008).
[33] L. D. G. Sigalotti, H. López, and L. Trujillo, J. Comput. Phys. **228**, 5888 (2009).
[34] M. B. Liu and G. R. Liu, Arch. Comput. Methods Eng. **17**, 25 (2010).
[35] J. Bonet and T.-S. L. Lok, Comput. Methods Appl. Mech. Eng. **180**, 97 (1999).
[36] A. N. Charles and P. Daivis, in *Proceedings of the 19th International Congress on Modelling and Simulation (MODSIM11)*, edited by F. Chan, D. Marinova, and R. S. Anderssen (The Modelling and Simulation Society of Australia and New Zealand, Canberra, Australia, 2011), pp. 516–522.
[37] M. Jubelgas, V. Springel, and K. Dolag, Mon. Not. R. Astron. Soc. **351**, 423 (2004).
[38] L. Brookshaw, Proc. Astron. Soc. Australia **6**, 207 (1985).
[39] M. Yildiz, R. A. Rook, and A. Suleman, Int. J. Numer. Methods Eng. **77**, 1416 (2009).
[40] J. P. Morris, P. J. Fox, and Y. Zhu, J. Comput. Phys. **136**, 214 (1997).
[41] D. Zhou, S. Chen, L. Li, H. Li, and Y. Zhao, Eng. Appl. Comput. Fluid Mech. **2**(2), 244 (2008).
[42] L. B. Lucy, Astron. J. **82**, 1013 (1977).
[43] D. J. Price, PASA **24**, 159 (2007).
[44] A. R. Imre, A. Drozd-Rzoska, A. Horváth, T. Kraska, and S. J. Rzoska, J. Non-Cryst. Solids **354**, 4157 (2008).
[45] M. Mecke, J. Winkelmann, and J. Fischer, J. Chem. Phys. **107**, 9264 (1997).
[46] M. P. Moody and P. Attard, J. Chem. Phys. **115**, 8967 (2001).
[47] W. C. Reynolds, *Thermodynamic Properties in SI* (Stanford University Press, Stanford, CA, 1979).
[48] J. Winkelmann, J. Phys.: Condens. Matter **13**, 4739 (2001).
[49] M. N. Berberan-Santos, E. N. Bodunov, and L. Pogliani, J. Math. Chem. **43**, 1437 (2008).